Repetitive formation and decay of current sheets in magnetic loops: An origin of diverse magnetic structures

Dinesh Kumar[1], R. Bhattacharyya[1], and P. K. Smolarkiewicz[2]

[1] *Udaipur Solar Observatory, Physical Research Laboratory, Dewali, Bari Road, Udaipur-313001, India and*

[2] *European Centre for Medium-Range Weather Forecasts, Reading RG2 9AX, UK.*

(Dated: December 3, 2014)

Abstract

In this work, evolution of an incompressible, thermally homogeneous, infinitely conducting, viscous magnetofluid is numerically explored as the fluid undergoes repeated events of magnetic reconnection. The initial magnetic field is constructed by a superposition of two linear force-free fields and has similar morphology as the magnetic loops observed in the solar corona. The results are presented for computations with three distinct sets of footpoint geometries. To onset reconnection we rely on numerical model magnetic diffusivity, in the spirit of Implicit Large Eddy Simulation (ILES). It is generally expected that in a high Lundquist number fluid, repeated magnetic reconnections are ubiquitous and hence can lead to a host of magnetic structures with considerable observational importance. In particular, the simulations presented here illustrate formations of magnetic islands, rotating magnetic helices and rising flux ropes — depending on the initial footpoint geometry but through the common process of repeated magnetic reconnections. Further, we observe development of extended current sheets in two case studies, where the footpoint reconnections generate favorable dynamics.

PACS numbers: 52.25.Xz, 52.30.Cv, 52.35.Vd, 95.30.Qd

Keywords: MHD, Current Sheet, EULAG, Solar/Stellar atmosphere

I. INTRODUCTION

The generation of tangential discontinuities (TDs) in magnetic field ($\mathbf{B}$), or equivalently current sheets (CSs), and their subsequent decay through magnetic reconnection (MR) is responsible for a multitude of solar/stellar eruptive phenomena in the likes of flares and coronal mass ejections (CMEs). The MR is a diffusive process which changes the topology of magnetic field lines while simultaneously accelerating the magnetofluid. The irreversible dissipation of magnetic energy to heat is a possible cause to maintain the solar corona at its million degree Kelvin temperature [1].

The diffusive and the non-diffusive limits of magnetohydrodynamics (MHD) are determined by the Lundquist number $S \equiv \tau_D/\tau_A$, where τ_D and τ_A are the diffusion and Alfvén transit times

$$\tau_D = \frac{L^2}{\eta} \quad , \tag{1}$$

$$\tau_A = \frac{L}{V_A} \quad , \tag{2}$$

in a magnetofluid with an Alfvén speed $V_A = B_0/\sqrt{4\pi\rho_0}$, length scale L and magnetic diffusivity η. The constants ρ_0 and B_0 are the ambient mass density and magnetic field respectively.

The astrophysical magnetofluids have a high Lundquist number ($S \approx 10^{10}$) because of the large length scales involved, and hence can be approximated by the non-diffusive limit of the MHD for all practical purposes. In this limit, magnetic field lines are tied to the fluid parcels — a condition referred to as the "frozen-in" or "flux-freezing" [2]. In a recent work of Kumar et al. [3], this condition of flux-freezing is used to numerically demonstrate spontaneous development of CSs when an incompressible and thermally homogeneous magnetofluid with periodic boundaries, is allowed to undergo a viscous relaxation to a terminal quasi-steady state. The mainstay of this demonstration is in its realization that a magnetofluid under flux-freezing can be divided into contiguous sub-volumes where each sub-volume entraps its own magnetic flux. In presence of a Lorentz force, these magnetic sub-volumes are convected with the flow. Consequently, by ejecting out a third interstitial sub-volume, two sub-volumes which were initially apart can come arbitrarily close to each other enabling the otherwise negligible magnetic diffusivity to become effective through a local reduction in S. The

magnetic field lines (MFLs) then diffuse from one sub-volume to the other, leading to MRs if the two interacting sub-volumes have a favorable geometry of oppositely directed MFLs. Under the condition of $\eta = 0$, the diffusion of field lines across the two interacting sub-volumes is prohibited. The component of magnetic field tangential to the common surface of interaction then becomes discontinuous — developing the tangential discontinuity (TD). From Ampere's law, the volume current density $\mathbf{J} = \nabla \times \mathbf{B}$ is then intensified and contained wholly on the surface across which the magnetic field is discontinuous. This intense current is called a current sheet, because of its two dimensional appearance.

The above rationale finds support from the optical analogy introduced by Parker [4–6]. In its skeletal form, the analogy uses the similarity of field line equations of a potential field $\mathbf{B}_P$ on a flux surface Γ with the path of optical rays in a medium of refractive index $\mid \mathbf{B}_P \mid$. The field lines on Γ then stream according to Fermat's principle and get refracted away from a sufficiently local maximum of $\mid \mathbf{B}_P \mid$, opening up a gap on the surface S. In a stack of such flux surfaces then these individual gaps extend to a hole. Magnetic field lines from regions which are at the top and bottom of the stack then enter thorough this hole and forms a CS when pushed by a Lorentz force as the intruding field lines are in general not parallel. Although stated here for a potential field, an extension to include more general magnetic fields is straightforward and can be found in [1, 3].

However, in reality the astrophysical magnetofluids are characterized with a small but non-zero magnetic diffusivity. Recall that a typical value of S is approximately 10^{10}, but not infinite. Once developed, a CS then provides a site where S is sufficiently reduced through the decrease of L enabling the magnetofluid to become locally diffusive. The resulting MR is then localized in space and decay out the CS. Once the CS is decayed, the characteristic scale L becomes once again large and the post-reconnection MFLs are frozen to the reconnection outflow. These MFLs with their changed topology are then expected to push further onto field lines located away from the primary reconnection site, eventually leading to secondary reconnections due to local reduction of S at new sites. Furthermore, the changed topology of MFLs defines new contiguous sub-volumes entrapping the magnetic flux, thus enabling new sub-volumes coming into a contact by ejecting interstitial mass. Altogether, this culminates into a series of MR events altering the dynamics repetitively in time. Presumably, this process occurs until the total ordered energy of the magnetofluid achieves an allowable lower limit; e.g., as in the Taylor relaxation [7] mediated via MRs, where the lower bound of

the total ordered energy in the absence of flow is constrained by an approximate preservation of magnetic topology. Clearly, it is imperative to explore the importance of repeated MRs in shaping up the global dynamics of the magnetofluid.

A successful numerical simulation in this direction primarily requires satisfaction of the flux-freezing to a high fidelity in between two consecutive MRs. The other requirement is the presence of a magnetic diffusivity, localized and concurrent with diminishing of L, to onset reconnection. To achieve these requirements, we propose the following hybrid numerical scheme which utilizes a seamless transition from Direct Numerical Simulation (DNS) to Implicit Large Eddy Simulation (ILES) and back.

To focus on the idea, we consider non-resistive evolution of a magnetofluid toward a terminal state characterized by local force balance — an analytical condition for CSs to form [8, 9]. Based on our previous experiences, an apt computational scheme for the case is then to perform DNS of an incompressible, thermally homogeneous magnetofluid with an infinite electric conductivity, as it relaxes to a terminal quasi-steady state under the influence of viscosity. The dynamics is then governed by the relevant MHD equations

$$\rho_0 \left(\frac{\partial \mathbf{v}}{\partial t} + (\mathbf{v} \cdot \nabla)\, \mathbf{v} \right) = \mu_0 \nabla^2 \mathbf{v} + \frac{1}{4\pi} (\nabla \times \mathbf{B}) \times \mathbf{B} - \nabla p \quad , \tag{3}$$

$$\nabla \cdot \mathbf{v} = 0 \quad , \tag{4}$$

$$\frac{\partial \mathbf{B}}{\partial t} = \nabla \times (\mathbf{v} \times \mathbf{B}) \quad , \tag{5}$$

$$\nabla \cdot \mathbf{B} = 0 \quad , \tag{6}$$

in standard notations, where ρ_0 and μ_0 are uniform density and coefficient of viscosity respectively. In its analytical form, equation (6) is redundant in the sense that it is implied for all time by the induction equation (5) when the initial field is solenoidal. If released from an initial nonequilibrium state (cf. section II in [8]), this magnetofluid would ultimately relax toward a terminal equilibrium by converting magnetic energy W_M to kinetic energy W_K via equations

$$\frac{dW_K}{dt} = \int \frac{1}{4\pi} [(\nabla \times \mathbf{B}) \times \mathbf{B}] \cdot \mathbf{v} \; d^3x - \int \mu_0 \left| \nabla \times \mathbf{v} \right|^2 \; d^3x \quad , \tag{7}$$

$$\frac{dW_M}{dt} = - \int \frac{1}{4\pi} [(\nabla \times \mathbf{B}) \times \mathbf{B}] \cdot \mathbf{v} \; d^3x \quad , \tag{8}$$

$$\frac{dW_T}{dt} = - \int \mu_0 \left| \nabla \times \mathbf{v} \right|^2 \; d^3x \quad , \tag{9}$$

satisfying conditions that the net magnetic and velocity fluxes through the boundaries of the computational domain are individually zero. The Lorentz force being conservative, only irrecoverable loss of energy is by the viscous drag. An approximate balance between the Lorentz force, pressure gradient and the viscous drag then determines the quasi-steady terminal state characterized by a small kinetic energy. The magnetic field being frozen, it cannot decay to zero, and CSs are expected to develop as the magnetofluid relaxes to this terminal state. Consequently the magnetic field gradient sharpens locally up to a threshold determined by the grid resolution and numerical techniques employed. This process generates under-resolved scales, with associated numerical artifacts such as spurious oscillations. In standard large eddy simulation, the under-resolved scales are filtered out with the aid of explicit subgrid-scale models. An alternative and effective way of filtering out the under-resolved scales is to utilize the apt numerical diffusivity of nonoscillatory finite-volume differencing, mimicking the action of explicit subgrid scale turbulence models. In literature, such calculations relying on the properties of nonoscillatory numerics are referred as implicit large-eddy simulations (ILESs) [10]. The dissipation of under-resolved scales through this diffusivity then results in MRs that are co-located and concurrent with the CSs. Post reconnection, the field is well resolved so the computation is back again in its DNS mode, and allows for further development of CSs as the field lines frozen in the reconnection outflow push onto another set of MFLs. Such seamless transitions from a DNS to an ILES and back, then imitates physical MRs in a high Lundquist number magnetofluid in terms of being co-located and concurrent to the development of CSs — opening up a way to explore formation of CSs and their influence on magnetofluid evolution through repetitive MR events.

In this work we extend simulations of Kumar et al. [3] to study the dynamics of a magnetofluid undergoing repetitive MRs, achieved by the properties of nonoscillatory numerics inherent to our computational model. The initial magnetic field is so selected that it allows for an interaction between two sets of MFLs, where each set is morphologically similar to the magnetic loops observed in the solar corona. The crucial finding of this paper is in the demonstration of complex magnetic structures: magnetic island, twisted flux rope and magnetic helices, through the common process of repetitive MRs.

The paper is organized as follows. The numerical model and the initial state are discussed in sections II while simulation results are presented in section III. Section IV summarizes these results.

II. NUMERICAL MODEL AND THE INITIAL STATE

The equations (3) to (6) are solved using the well established magnetohydrodynamic model EULAG-MHD [11] based entirely on the spatio-temporally second order accurate nonoscillatory forward-in-time advection scheme MPDATA (for *multidimensional positive definite advection transport algorithm*) [12]. The EULAG-MHD is a spin-off of the numerical model EULAG [13], predominantly used in atmospheric and climate research. To minimize the text, here we only summarize the features of EULAG-MHD important to our study. For further details the interested reader is referred to [11] and references therein.

A feature unique to MPDATA and important in our computation is its proven dissipative property, intermittent and adaptive with loss in resolution of field variables. Within our framework of viscous relaxation leading to CS formation, such loss in resolution and development of under-resolved scales are inevitable as the magnetic field gradient grows unboundedly. This insufficient resolution in presence of locally high gradient of $\mathbf{B}$ then triggers concurrently MPDATA residual dissipation (of the second-order in grid resolution) sufficient to maintain solution monotonicity — a feature well documented in literature [14]. The intermittency and adaptiveness in generation of this residual dissipation (along with its consequence for a transition from DNS to ILES) has already been well established for hydrodynamic simulations [15]. In computations carried out here, we rely on this property of MPDATA to onset reconnection. To strengthen our case further, we note that a series of recent computations have successfully used the EULAG-MHD in its ILES mode. For example, Ghizaru and coworkers have successfully simulated regular solar cycles [16] while rotational torsional oscillations in a global solar dynamo has been characterized and analyzed utilizing the ILES scheme of EULAG-MHD [17]. The present understanding along with open questions on modeling the solar dynamo are summarized in [18].

As a continuation of our earlier work, here we construct the initial magnetic field by superposing two linear force-free fields (lfffs) $\mathbf{B}_1$ and $\mathbf{B}_2$. The superposed field $\mathbf{B}'$ is then given by

$$\mathbf{B}' = \mathbf{B}_1 + \gamma \mathbf{B}_2 \quad , \tag{10}$$

where the constant factor γ relates the amplitudes of $\mathbf{B}_1$ and $\mathbf{B}_2$ and represents the deviation of $\mathbf{B}'$ from the force-free configuration. The fields $\mathbf{B}_1$ and $\mathbf{B}_2$ satisfy

$$\nabla \times \mathbf{B}_1 = \alpha_1 \mathbf{B}_1 \quad , \tag{11}$$

$$\nabla \times \mathbf{B}_2 = \alpha_2 \mathbf{B}_2 \quad , \tag{12}$$

with torsion coefficients α_1 and α_2 representing magnetic circulations per unit flux for $\mathbf{B}_1$ and $\mathbf{B}_2$ respectively [19]. Noting that the eigenfunctions of the operator $\nabla\times$ form a complete orthonormal basis [20], the above choice of $\mathbf{B}'$ is a natural selection for the initial magnetic field because of the prospect of having MFLs which are geometrically similar to the field lines of the more traditional lfff approximation of the solar corona. In addition, as pointed out in [3, 21], the superposed field has a possible relevance in CS formation through the process of magnetic flux emergence. The Lorentz force exerted by $\mathbf{B}'$ is

$$\mathbf{J}' \times \mathbf{B}' = \frac{1}{\mu}\gamma(\alpha_1 - \alpha_2)\mathbf{B}_1 \times \mathbf{B}_2 \ . \tag{13}$$

which is non-zero only for the simultaneous satisfaction of conditions $\alpha_1 \neq \alpha_2$ and $\gamma \neq 0$. A solution of equation (10) pertaining to the magnetic loops observed in the solar corona is obtained by following [22]. The components of $\mathbf{B}'$ for the positive half-space ($z \geq 0$) of a Cartesian coordinate system having periodicity along the laterals (x and y) are then

$$B'_x = B_0[(1+\gamma) \times \cos\left(x\sqrt{\frac{1+\alpha^2}{2}}\right) \cos\left(y\sqrt{\frac{1+\alpha^2}{2}}\right)$$
$$+\frac{(1-\gamma)(1+\alpha^2)}{2\alpha} \sin\left(x\sqrt{\frac{1+\alpha^2}{2}}\right) \sin\left(y\sqrt{\frac{1+\alpha^2}{2}}\right)] \exp(-z) \quad , \tag{14}$$

$$B'_y = B_0[(1-\gamma) \times \frac{\alpha^2-1}{2\alpha} \cos\left(x\sqrt{\frac{1+\alpha^2}{2}}\right) \cos\left(y\sqrt{\frac{1+\alpha^2}{2}}\right)] \exp(-z) \quad , \tag{15}$$

$$B'_z = -B_0\sqrt{\frac{1+\alpha^2}{2}}[(1+\gamma) \sin\left(x\sqrt{\frac{1+\alpha^2}{2}}\right) \cos\left(y\sqrt{\frac{1+\alpha^2}{2}}\right)$$
$$-\frac{1-\gamma}{\alpha} \cos\left(x\sqrt{\frac{1+\alpha^2}{2}}\right) \sin\left(y\sqrt{\frac{1+\alpha^2}{2}}\right)] \exp(-z) \quad , \tag{16}$$

where B_0 is an arbitrary constant amplitude. In deriving the above, we have taken the simplest choice of $\alpha_1 = -\alpha_2 = \alpha$ and the mode $k_x = k_y = k_z = 1$. Important from [22] is also the dependence of field line topology on the parameters α and γ. Noting this importance, in the following we discuss three cases of gradually increasing geometric complexity, with the

interacting sets of MFLs of $\mathbf{B}'$ characterized by different values of α and γ and, thus, distinct topology and footprint geometry. The case i is the simplest, assuming mirror symmetry and untwisted field lines. In the case ii, the mirror symmetry of the case i is disturbed by a relative translation of the reflected MFLs (hereafter, glide symmetry) yet the field lines are kept untwisted. The translation is so chosen as to keep the amplitude of the magnetic field at $z = 0$ plane equal but opposite in sign, before and after the symmetry operation. Finally, in case iii the glide symmetry is maintained but the field lines are twisted.

A. Case i: $\alpha = 1$ and $\gamma = 1$

With B_0 set to 0.5, the components of $\mathbf{B}'$ are then

$$H_x^1 = \cos(x)\cos(y)\exp(-z) \quad , \tag{17}$$

$$H_y^1 = 0 \quad , \tag{18}$$

$$H_z^1 = -\sin(x)\cos(y)\exp(-z) \quad . \tag{19}$$

The differential equation satisfied by the field lines of a general magnetic field $\mathbf{B}$ in Cartesian coordinates being

$$\frac{dx}{ds} = \frac{B_x}{\mid \mathbf{B} \mid} \quad , \tag{20}$$

$$\frac{dy}{ds} = \frac{B_y}{\mid \mathbf{B} \mid} \quad , \tag{21}$$

$$\frac{dz}{ds} = \frac{B_z}{\mid \mathbf{B} \mid} \quad , \tag{22}$$

with ds as the invariant length; the magnetic field lines of $\mathbf{H}^1$ are tangential to y-constant surfaces, as depicted in panel a of figure 1. In this and subsequent figures, the arrows in colors red, green and blue represent the directions x, y, and z respectively. In different illustrations presented in this paper, generally the y direction is restricted to [0, π] since similar structure and dynamics is repeated in the region [π, 2π]. Also, The existence of two field reversal layers at $y = \pi/2$ and $y = 3\pi/2$ is evident from equations (17) — (19). The polarity inversion lines (PILs), defined as the lines on which $B_z = 0$ on the $z = 0$ plane, are straight lines; located at $x = \pi$ and are perpendicular to the field reversal layers.

The field lines being co-planar with y-constant planes, are untwisted and exert a Lorentz force $\mathbf{L}^1$

$$L_x^1 = 0 \quad , \tag{23}$$

$$L_y^1 = 2\sin(y)\cos(y)\exp(-2z) \quad , \tag{24}$$

$$L_z^1 = 0 \quad . \tag{25}$$

Two observations are noteworthy. In contrast to the periodic solutions used in [3], the bipolar field lines lack any two or three dimensional neutral point. Second, the location of footpoints (intersections of field lines with the $z = 0$ plane) with opposite polarities satisfy mirror symmetry across the field reversal layers. For better clarity, in panel b we depict projections of two field lines situated at either side of the field reversal layer at $y = \pi/2$, on the $z = 0$ plane. The corresponding pairs of footpoints are denoted by symbols A, A' and B, B' respectively. These projections being straight lines, additionally confirms $\mathbf{H}^1$ to be untwisted. Further, both panels are overlaid with contours of H_z^1 to depict polarities of footpoints located at different regions.

B. Case ii. $\alpha = 1$ and $\gamma = 0.8$

We set the amplitude $B_0 = 0.5$. The corresponding $\mathbf{B}'$, termed $\mathbf{H}^2$, then has components

$$H_x^2 = [0.9\cos(x)\cos(y) + 0.1\sin(x)\sin(y)]\exp(-z) \quad , \tag{26}$$

$$H_y^2 = 0 \quad , \tag{27}$$

$$H_z^2 = -[0.9\sin(x)\cos(y) - 0.1\cos(x)\sin(y)]\exp(-z) \quad . \tag{28}$$

and yields a Lorentz force

$$L_x^2 = 0 \quad , \tag{29}$$

$$L_y^2 = 1.6\sin(y)\cos(y)\exp(-2z) \quad , \tag{30}$$

$$L_z^2 = 0 \quad . \tag{31}$$

Figure 2, panel a, illustrates the magnetic field lines of $\mathbf{H}^2$ overlaid with contours of H_z^2 at the $z = 0$ plane. From the figure, it is explicit that the field lines are untwisted as before — once again because of $H_y^2 = 0$, but in contrast to the Case i the PILs are curved lines. While constructing the field lines, the glide symmetry is ensured by demanding the footpoints reflected about the $y = \pi/2$ plane to be relatively displaced by an amount Δx in the x-direction, implying the identities

$$H_x^2(x, y, 0) = -H_x^2(x + \Delta x, \pi - y, 0) \quad , \tag{32}$$

$$H_z^2(x, y, 0) = -H_z^2(x + \Delta x, \pi - y, 0) \quad , \tag{33}$$

to make $|\mathbf{H}^2|_{z=0}$ equal for a pair of opposite polarity footpoints, before and after the symmetry operation. To calculate this Δx we plot variations of $H_x^2(x, y, 0)$ and $-H_x^2(x, \pi - y, 0)$ with x, for a given y. The plots then generate two spatially shifted sinusoidal curves, illustrated in panel b of Fig. 2. We then identify the Δx with this spatial shift — the offset required to exactly superimpose one curve on the other. A similar procedure using plots of $H_z^2(x, y, 0)$ and $-H_z^2(x, \pi - y, 0)$ yields the same Δx. The MFLs illustrated in panel a of figure 2 are constructed with $y = 2\pi/5$ and a relative displacement $\Delta x = \pi/5$. The presence of an identical glide plane at $y = 3\pi/2$ is apparent because of the periodicity in the y-direction.

C. Case iii. $\alpha = \sqrt{7}$ and $\gamma = .5$

The components of $\mathbf{B}'$, with a selection of $B_0 = 1$, are

$$H_x^3 = [1.5\cos(2x)\cos(2y) + \frac{2}{\sqrt{7}}\sin(2x)\sin(2y)]\exp(-z) \quad , \tag{34}$$

$$H_y^3 = [\frac{1.75}{\sqrt{7}}\cos(2x)\cos(2y)]\exp(-z) \quad , \tag{35}$$

$$H_z^3 = -[3\sin(2x)\cos(2y) - \frac{1}{\sqrt{7}}\cos(2x)\sin(2y)]\exp(-z) \quad . \tag{36}$$

exerting a Lorentz force

$$L_x^3 = [-12\sin(2x)\cos(2x)\cos^2(2y)]\exp(-2z) \quad , \tag{37}$$

$$L_y^3 = [4\sin(2y)\cos(2y)1 + 3\sin^2(2x)]\exp(-2z) \quad , \tag{38}$$

$$L_z^3 = [-12\cos^2(2x)\cos^2(2y)]\exp(-2z) \quad , \tag{39}$$

the lateral components of which at the $z = 0$ plane are plotted in panel d of figure 2. The selection of $\alpha = \sqrt{7}$ is made to keep the computational domain size and hence, the fluid Reynolds number R_F, same as in the previous cases while maintaining the periodicity of the lateral boundaries. The magnetic field lines are illustrated in panel c of figure 2. As oppose to the cases i and ii, $H_y^3 \neq 0$ makes the field lines twisted and hence, their projections on the $z = 0$ plane are curved lines (Fig. 2, panel c). Also, similar to the earlier case, the opposite polarity footpoints satisfy a glide symmetry where one of the reflection planes is located at $y = \pi/4$ and the translation Δx is determined by the identities

$$H_x^3(x, y, 0) = -H_x^3(x + \Delta x, \pi/2 - y, 0) \quad , \tag{40}$$

$$H_z^3(x, y, 0) = -H_z^3(x + \Delta x, \pi/2 - y, 0) \quad . \tag{41}$$

Following the procedure employed in case ii, auxiliary calculations (not presented here) give $\Delta x = \pi/20$ for footpoint coordinate $(x, y, 0) = (4\pi/5, 7\pi/20, 0)$. The other glide planes are located at $y = 3\pi/4, 5\pi/4,$ and $7\pi/4$.

We consider the fields $\mathbf{H}^1$, $\mathbf{H}^2$ and, $\mathbf{H}^3$ as the initial magnetic fields for computations presented in this paper.

III. RESULTS AND DISCUSSIONS

The simulations are carried out in the $(2\pi)^3$ m^3 domain, resolved with 96^3 uniform grid intervals $\Delta x = \Delta y = \Delta z = 2\pi/95$. The duration times of the simulations for the cases i, ii, and iii, respectively, $T = 48, 128, 128$ s, are resolved with the same temporal increment $\delta t = 0.032$ s. The density is set to $\rho_0 = 1$ kg m^{-3} and $\mu_0 = 0.004$ m^2 s^{-1}. For the field initial conditions specified in (17)-(19), (26)-(28) and (34)-(36), the magnetofluid is evolved from states of rest — with $(\nabla \times \mathbf{B}) \times \mathbf{B}/(4\pi) - \nabla p \neq 0$ in (3) — via viscous relaxation; cf. Section 5 in [24]. The lateral boundaries are selected to be periodic, whereas the vertical boundary is open. The normal component of mass and magnetic flux at each boundary is kept fixed to zero.

To compare our simulations with the solar corona, we note that the relevant MHD equations in absence of any dissipation are independent of both temporal and spatial scales under the following transformations

$$\mathbf{B} \longrightarrow \frac{\mathbf{B}}{B_0} \quad , \quad \nabla \longrightarrow \frac{\nabla}{L} \quad , \tag{42}$$

$$\mathbf{v} \longrightarrow \frac{\mathbf{v}}{V_A} \quad , \quad t \longrightarrow \frac{t}{\tau_A} \quad , \tag{43}$$

where the constants L and B_0 are in general arbitrary but, also can be equated to the characteristic length and the ambient magnetic field respectively. In presence of viscosity and resistivity the scale dependencies are essentially clumped into the dimensionless numbers S and τ_A/τ_v, where $\tau_v = L^2/\nu_0$ with ν_0 being the kinematic viscosity. The deviations of our simulations from the corona then would only be reflected in the numerical values of these two dimensionless numbers. We further note that in our computations, S is effectively infinite except for the locations of MRs. The residual dissipation responsible for these MRs being intermittent in time and space, a quantification of it is only meaningful in the spectral space, where — in analogy to the eddy-viscosity of explicit subgrid-scale models for turbulent flows — it only acts on the shortest modes admissible on the grid [23]; in particular, in the vicinity of steep gradients in simulated fields. Also, in these computations $\tau_A/\tau_v \approx 10^4$, whereas an approximate value of the same parameter in the corona is 2.5×10^3. This deviation in τ_A/τ_v only affects the time scale over which the magnetofluid evolves and has no direct consequence on the change in magnetic topology. The assumptions of constant ρ_0 and thermal homogeneity are also not compatible with the actual corona. Altogether then, the relevance of our computations to different coronal structures are only in terms of their similarities in magnetic topology.

Against the above backdrop, the results of the simulations for the three cases are presented in the following.

A. Case i. $\alpha = 1$ and $\gamma = 1$

The overall dynamics of the magnetofluid is demonstrated by the plot of normalized kinetic energy with time (Fig. 3). The development of the peak, located at $t \approx 8$ s, is attributed to an arrest of magnetofluid acceleration by viscous drag. Noticeable is the

quasi-steady phase of the evolution, approximately coinciding with the period $t \in (24, 32)$ s. The figure 4 illustrate snapshots of field lines in their important phases of evolution.

To facilitate an understanding of the magnetofluid dynamics, we refer to panel b of figure 1. From equations (23)-(25), the initial Lorentz force $\mathbf{L}^1$ acting along the y-direction, pushes the field lines with footpoint pairs AA' and BB' simultaneously toward the field reversal layer at $y = \pi/2$. Since the magnitude of $\mathbf{L}^1$ for a given field line is maximum at the footpoints (from equations (23)–(25)), the relative approach of any other mirror symmetric points lying on field lines joining A, A' and B, B' is slower than the relative approach of A toward B and A' toward B'. As a result, two simulatenous reconnections take place between A, B and A', B'; onset by a local sharpening of field gradient — indicated by the rise and fall of the electric current density at the field reversal layer (Fig. 5) before and after the reconnections. Such reconnections repeated in time then culminate into generating a magnetic island, complete with the development of two X-type nulls — marked in the figure 4 (panel b) by the symbol $X1$. It is important to note that the post-reconnection open field lines are of quadrupolar geometry. Also from panels c and d, it is apparent that the concavity of the open field lines increases concurrently with an increase in the number of closed field lines constituting the island. Since an increase in number of closed field lines intensifies $\mid \mathbf{H}^1 \mid$ at the island, the increased concaveness of open field lines is then a direct consequence of the Parker's optical analogy.

In figure 6 we present MFLs at instances $t = 1.2$ s, $t = 6$ s, and $t = 12$ s, projected on the $x = 3\pi/2$ plane. The separatrices are drawn in color magenta. Noticeable is the ascend of this X-type neutral point in the vertical direction along with a concurrent increment of the separation between footpoints of the reconnected field lines below the X-type null. Such an ascend of X-type neutral point is also observed in the context of solar flares [25, 26]. A plausible rationale for this ascend, within the scope of our computation is presented in the following. In our scenario of repeated reconnections, at the initial stages of its evolution, the magnetic island is always pushed at immediate neighborhood of the X-type nulls by the subsequently reconnected field lines. The resulting compression then accounts for the observed ascend. Also the compression being volume preserving because of the solenoidality of flow, the magnetic island becomes more circular with the ascend and, generates a O-type neutral line at $x = \pi, y = \pi/2$ oriented along the z-direction. This circular island then further shrinks self-similarly and decays away at the O-type neutral line (panels d, e and

f of Fig. 4). As a consequence, the local magnetic pressure decreases and the open field lines oriented along the y direction invade this free space to form a new X-type neutral point (marked by the symbol $X2$), as demonstrated in panel g of figure 4. To explore the subsequent dynamics generated by continuous squashing of this new X-type null, in figure 7 we present the top view of MFL evolution at instances $t = 15$ s and $t = 26$ s. From this top view, the generation of two Y-type nulls and an extended CS (panel b) is obvious. Noteworthy is the approximate simultaneity of the development of this extended CS with the quasi-steady phase of evolution $t \in (24, 32)$ s, in agreement to one of the analytical requirements of CS formation. Further pushing of field lines then decay this extended CS through MRs, not shown here to keep the number of figures at minimum.

B. Case ii. $\alpha = 1$ and $\gamma = 0.8$

The general evolution of the fluid follows the normalized kinetic energy curve plotted in figure 8. The evolution can clearly be divided into the three following phases. The first phase is characterized by a peak, centered at $t \approx 10$ s, developed as the initial increase in kinetic energy is halted by viscous drag. The second phase is approximately quasi-steady and ranges from $t \in (53, 75)$ s; whereas the third phase shows a monotonic decay of kinetic energy.

The time sequence of MFLs are shown in panels a to f of figure 9. The noteworthy is the development of funnel-shaped helical magnetic field lines (most prominent at $t = 44$ s), akin to the tornadoes observed at the solar atmosphere. This development of helical field lines coincides with the first phase of the kinetic energy evolution. In panels d and e, we depict a rotation of field lines in a direction opposite to the developed helix. This "untwisting" motion overlaps with the second phase and then decays out eventually. Also noticeable is the absence of extended CSs generated during the evolution.

To elucidate the relevant dynamics of footpoints, in figure 10 we present a schematic of two sets of six initial footpoints lying on the two opposite sides of the glide symmetric plane represented by the central line. The corresponding magnetic field lines then lie on two glide symmetric y-constant planes and are of different heights. The relative polarity of the footpoints are marked by arrows while the length of an arrow measures the intensity of the corresponding magnetic field. The footpoints of field lines with different heights are shifted

laterally to further enhance the clarity of the schematic. The three pairs of footpoints for the depicted field lines are nomenclatured as A, A'; B, B'; C, C'; D, D'; E, E'; and F, F'.

From equation (29), the initial Lorentz force $\mathbf{L}^2$ being in the direction y with a sign flip at $y = \pi/2$ – presses the glide-symmetric opposite polarity footpoints toward the $y = \pi/2$ line. This pressing is periodic in the x- direction, being maximum at the two lateral boundaries and zero at the $x = \pi$ plane. In response the footpoints A and E reconnect first, followed by reconnection between E' and C'. The final reconnected field line then, is of the form of a spiral — the projection of which on the $z = 0$ plane traces out a helical path in the direction of $CC'E'EAA'$ as illustrated in panel b of figure 10. It is also to be noted that a similar helix with the same chirality develops through footpoint reconnections in the sequence of $F', B'; B, D$. In figure 11, we display the evolution of two such helices projected on the $z = \pi/2$ plane. The spirals marked by the two different colors (red and cyan) correspond to the two helices described above. In panels e and f we depict these spirals at the instances $t = 55$ s and $t = 65$ s coinciding with the quasi-steady phase of the kinetic energy plot. As the spirals maintain their original chirality, two neighboring field lines are always directed along the same direction — prohibiting formation of extended CSs in absence of a favorable magnetic geometry.

The helical motion of the magnetofluid is further illustrated in figure 12 through the image-based flow visualization technique [27], presented for different vertical levels overlaid with velocity field lines. In confirmation to the twisting motion and the resulting funnel-shape, the figure clearly shows swirls of magnetofluid with size increasing along the vertical.

Moreover, the simulated untwisting motion of previously twisted magnetic field lines (panels e and f) have also been observed in solar tornadoes [28]. For a plausible mechanism of this untwisting motion, we recognize that a viscously damped torsional Alfven wave propagating along the vertical is generated by rotation of field lines with a given chirality. The resulting increase in intensity of the lateral component of magnetic field at a z-constant plane then increases the corresponding magnetic pressure. This increased magnetic pressure pushes out the neighboring magnetic field lines more toward the reconnection regions resembling X-type neutral points situated on the z-constant plane — marked by rectangular patches centered at $(x, y) = (\pi, \pi/2), (\pi, 3\pi/2), (0, \pi/2), (0, 3\pi/2)$ (Fig. 13). The subsequent magnetic reconnections then generate counter-clockwise motion of the magnetic field lines as indicated from the plot of the velocity field lines shown in figure 12. Because of this

counter-clockwise motion, magnetic field lines first untwist, and then subsequently develop twist with an opposite chirality as demonstrated in figure 9.

C. Case iii. $\alpha = \sqrt{7}$ and $\gamma = 0.5$

The overall evolution of the fluid is represented by the history of normalized kinetic energy, plotted in panels a and b of figure 14. Based on these plots, the dynamics of the fluid can coarsely be separated out into four overlapping periods ranging from $t \in (0, 44)$ s, $t \in (44, 72)$ s, $t \in (72, 109)$ s and $t \geq 109$ s. The formation of the first peak in kinetic energy (panel a) is attributed once again to a viscous arrest of increasing kinetic energy of the fluid. Also to be observed are the quasi-steady evolution in the period $t \in (44, 72)$ s, and formation of a second peak in kinetic energy at $t \in (72, 109)$ s.

In figure 15 we depict topologies of evolving MFLs in the period $t \in (0, 51)$ s which overshoots into the onset of the quasi-steady phase. Noteworthy in the depictions is the generation of MFLs which are detached from $z = 0$ plane and are topologically similar to magnetic flux rope. Because of the inherent complexity in constructing three dimensional field line plots, the subsequent evolution of MFLs is described in figure 16 in terms of their projections on different x-constant planes. The corresponding time period include the quasi-steady phase and the formation of second peak in kinetic energy. An important feature in this period is the formation of an extended CS, depicted by contours of $\mid \mathbf{J}^3 \mid$ in color green, which increases in length along with a simultaneous rise of the flux rope (panels c to d).

Toward an explanation of the evolution, from the expression of the Lorentz force $\mathbf{L}^3$ we note that its direction at the footpoints for any pair of two opposite polarity glide symmetric magnetic field lines about the constant planes $y = \pi/4, 3\pi/4, 5\pi/4, 7\pi/4$, is not favorable for MRs. Instead, $\mathbf{L}^3$ favors a pair of same polarity glide symmetric magnetic field lines to be pushed toward each other. To explore the underlying dynamics then, we consider a set of selected glide symmetric magnetic field lines with the same polarity and located across the glide planes $y = 3\pi/4$ and $y = 5\pi/4$. The field lines represented by the color magenta join two footpoint regions with larger H_z^3 than the inner field lines represented by the color gray. From figure 2 panel d, we note that the initial Lorentz force pushes the inner field lines in the general direction of the glide planes at $y = 3\pi/4$ and $y = 5\pi/4$. The resulting increase in gradient of H_z^3 of two oppositely directed magnetic field lines then

causes MRs. The reconnected field lines lying above and below the reconnection region (marked as R), are shown in gray and cyan respectively — in the panel b of the figure 15. It is to be noted that with the rise of a reconnected field line above the region R (represented in gray), the footpoints of its two neighboring reconnected field lines are also simultaneously being pushed in the direction of the concave side of the rising field line. Because of this push, the neighboring reconnected field lines bulge toward the region R, as depicted in panel c. Successive MRs of the inner field lines then bring two such bulged field lines arbitrarily close to each other, leading to further reconnections. The reconnections of the bulged field lines result in generating the detached field lines which are concave away from the negative z-direction and thus have a magnetic tension directed along the vertical. This magnetic tension then upwells a detached field line, resulting in a diminished field region which facilitates additional reconnection of bulged field lines. A repetition of the above sequence of MRs then develop the bunch of detached helical magnetic field lines which resembles a flux rope. A well developed set of such helical field lines (in color cyan) is shown in panel d of figure 15. We must mention here that a strict mathematical description of flux rope as a stack of magnetic flux surfaces, requires the field lines to lie on the surface of the rope. A construction of flux surface is non-trivial in our computations which use advection of vector magnetic field. This non-triviality arises because of a general difficulty in separating out a field line that ergodically span a surface [29] from the one generated through post-processing errors. The equivalence of the detached, helical field lines observed in our computation to a flux rope is then only in an approximate sense. Also, noteworthy is the location of the flux rope which lies over the PIL. Such flux ropes located over PILs are widely believed to represent magnetic structures of solar prominences/filaments [30–32]. Moreover the repeated reconnections increase magnetic pressure of the flux rope which once exceed the magnetic tension of the overlying field lines, lifts the rope along the vertical. Subsequently, this lift translates into a sustained ascend of the flux rope (Fig. 16) maintained by an excess magnetic pressure; generated as field lines get bottle-necked below the rope. Also simultaneous to the ascend of the rope, this excess magnetic pressure drops because of a decrease in local density of field lines. The legs of the open MFLs are then sucked into this depleted field region to account for the formation of the extended CS and its continuous increase in extension. Interestingly, the appearance of the CS almost coincides with the steady phase of the evolution (Fig. 14). The second peak in kinetic energy is formed as the

upward motion of the rope is arrested by viscosity.

IV. SUMMARY

In this work, we explore asymptotic topologies of magnetic field lines shaped up by repeated events of magnetic reconnection using computations relying on the ILES property of nonoscillatory numerics. For the purpose, the initial magnetic field is constructed by a superposition of two linear force-free fields, solved appropriately in the $z \geq 0$ positive half-space of a partially periodic Cartesian coordinate system. This use of the positive half-space being traditional in mimicking the solar atmosphere, the computations presented here are of direct relevance to observations. Also the corresponding initial MFLs are of the form of loops, similar in geometry to the observed coronal loops.

The dynamics of these initial field lines are investigated in terms of their footpoint evolution with an objective to explore the development of physically realizable magnetic structures through the process of successive MRs. To be in conformity with the analytical requirements of CS formation, the magnetofluid is evolved from an unbalanced state of rest via viscous relaxation under the condition of flux freezing. In the process, magnetic field gradients sharpen unboundedly, ultimately generating under-resolved scales. These scales are then filtered out from the system through numerically assisted MRs. To regularize these reconnections, we rely on the proven dissipative property of MPDATA — the second order accurate advection scheme on which our computational model is based. Post MRs, the computations are again well-resolved and satisfy the condition of flux-freezing. The field lines frozen to the reconnection outflow then press onto other flux systems and repeat the above process. In particular, the paper explores this repetitive process for field lines characterized with three distinct cases of footpoint geometry.

In Case i, we choose the initial magnetic field to be untwisted with footpoints of opposite polarities satisfying a mirror symmetry and having straight PILs. The magnetofluid evolves with footpoint reconnections and leads to the formation of magnetic islands along with two X-type neutral points. Further, these X-type neutral points vertically ascend along with a simultaneous increase in separation between the footpoints of the underlying reconnected field lines — a phenomenon observed in the context of solar flares. More importantly, continual pressing of these islands develop a new pair of X-type neutral points which when

further squashed, generate two Y-type neutral points and an extended CS in accordance to the Parker's optical analogy.

The initial field lines in Case ii are also untwisted but characterized with curved PILs. The corresponding footpoints of opposite polarities satisfy a glide symmetry and hence are topologically more complex in comparison to the footpoints of Case i. The dynamics of the system is predominantly determined by the pressing of glide-symmetric footpoints toward each other. The resulting MRs impart a swirling motion of the magnetofluid along with the generation of helical magnetic field lines which are geometrically similar to the observed solar tornadoes. Additionally, the computations also confirm a later "untwisting" motion of these helical field lines as a consequence of repeated MRs. Such untwisting motions are also observational features of a solar tornado.

The Case iii investigates the evolution where the initial Lorentz force pushes two neighboring sets of twisted, glide-symmetric field lines. The repeated MRs in this case generate magnetic structure similar in appearance to a detached, twisted flux rope. The computations also suggest a sustained ascend of this flux rope driven by a difference in magnetic pressure, above and below the rope. Noteworthy is the development of an extended CS below the flux rope.

In retrospect, the importance of this work lies in its demonstration that different magnetic structures observed at the solar atmosphere can have a common origin in repeated MRs — sustained by an interplay of forcing and magnetic diffusion in a system of loops. Such repeated MRs (along with the prerequisite development of CSs), being fundamental to astrophysical plasmas; the resulting magnetic structures are expected to develop in other stellar coronae also. Moreover, we find that implicit large eddy simulations are capable to imitate MRs in a high Lundquist number magnetofluids in terms of their localized occurrences. On the flip side, such simulations, in absence of a physical magnetic diffusivity, provides no direct estimate of the reconnection rate. For completeness in understanding then, the results presented here require further investigation with an apt physical diffusivity. We keep this as a future assignment.

V. ACKNOWLEDEMENTS

The computations are performed using the High Performance Computing (HPC) cluster at Physical Research Laboratory, India. We also wish to acknowledge the visualisation software VAPOR (www.vapor.ucar.edu), for generating relevant graphics. One of us (PKS) is supported by funding received from the European Research Council under the European Union's Seventh Framework Programme (FP7/2012/ERC Grant agreement no. 320375).

---

[1] E. N. Parker, Spontaneous current sheets formation in magnetic fields (Oxford University Press, New York, 1994).

[2] D. Biskamp, Magnetic Reconnection in Plasmas (Cambridge Univ. Press, New York, 2000).

[3] D. Kumar, R. Bhattacharyya, and P.K. Smolarkiewicz, Phys. Plasmas **20**, 112903 (2013).

[4] E. N. Parker, Geophys. Astrophys. Fluid Dyn. **45**, 169 (1989).

[5] E. N. Parker, Geophys. Astrophys. Fluid Dyn. **46**, 105 (1989).

[6] E. N. Parker, Geophys. Astrophys. Fluid Dyn. **50**, 229 (1990).

[7] J. B. Taylor, Phys. Rev. Lett. **33**, 1139 (1974).

[8] R. Bhattacharyya, B.C. Low, and P.K. Smolarkiewicz, Phys. Plasmas **17**, 112901 (2010).

[9] E. N. Parker, Astronphys. **174**, 499 (1972).

[10] F. F. Grinstein, L. G. Margolin, and W. J. Rider, Implicit Large Eddy Simulation: Computing Turbulent Fluid Dynamics (Cambridge University Press, 2006).

[11] P. K. Smolarkiewicz and P. Charbonneau, J. Comput. Phys. **236**, 608 (2013).

[12] P. K. Smolarkiewicz, Int. J. Numer. Methods Fluids **50**, 1123 (2006).

[13] J. M. Prusa, P. K. Smolarkiewicz, and A. A. Wyszogrodzki, Comput. Fluids **37**, 1193 (2008).

[14] L. G. Margolin, W. J. Rider, and F. F. Grinstein, J. Turbul. **7**, N15 (2006).

[15] L. G. Margolin, P. K. Smolarkiewicz, and A. A. Wyszogradzki, J. Appl. Mech. **73**, 469 (2006).

[16] M. Ghizaru, P. Charbonneau, and P. K. Smolarkiewicz, Astrophys. J. Lett. **715**, L133 (2010).

[17] P. Beaudoin, P. Charbonneau, E. Racine, and P.K. Smolarkiewicz, Sol. Phys. **282**, 335 (2013).

[18] P. Charbonneau and P. K. Smolarkiewicz, Science, **340**, 42, 2013.

[19] E. N. Parker, Plasma Phys. Control. Fusion **54**, 124028 (2012).

[20] Z. Yoshida and Y. Giga, Math. Z. **204**, 235 (1990).

[21] B. Ravindra, P. Venkatakrishnan, Sanjiv Kumar Tiwari, and R. Bhattacharyya, Astrophys. J. **740**, 637 (2011).

[22] D. Kumar and R. Bhattacharyya, Phys. Plasmas **18**, 084506 (2011).

[23] A. Domaradzki, Z. Xiao, and P. K. Smolarkiewicz, Phys. Fluids **15**, 3890 (2003).

[24] J.-F. Cossette, P. K. Smolarkiewicz, and P. Charbonneau, J. Comput. Phys. **274**, 208 (2014).

[25] R. A. Kopp, and G. W. Pneuman, Sol. Phys. **50**, 85 (1976).

[26] S. Tsuneta, Astrophys. J. **456**, 840 (1996).

[27] J. J. van Wijk, ACM Transactions on Graphics, **21**, 745 (2002).

[28] Y. Su, T. Wang, A. Veronig, M. Temmer, and W. Gan, Astophys. J. **41**, 756 (2012).

[29] J. R. Jokipii and E.N. Parker, Astrophys. J. **155**, 777 (1969).

[30] S. F. Martin, Sol. Phys. **182**, 107 (1998).

[31] B. C. Low, J. Geophys. Res. **106**, 25141 (2001).

[32] Y. Fan and S. E. Gibson, Astrophys. J. **668**, 1232 (2007).

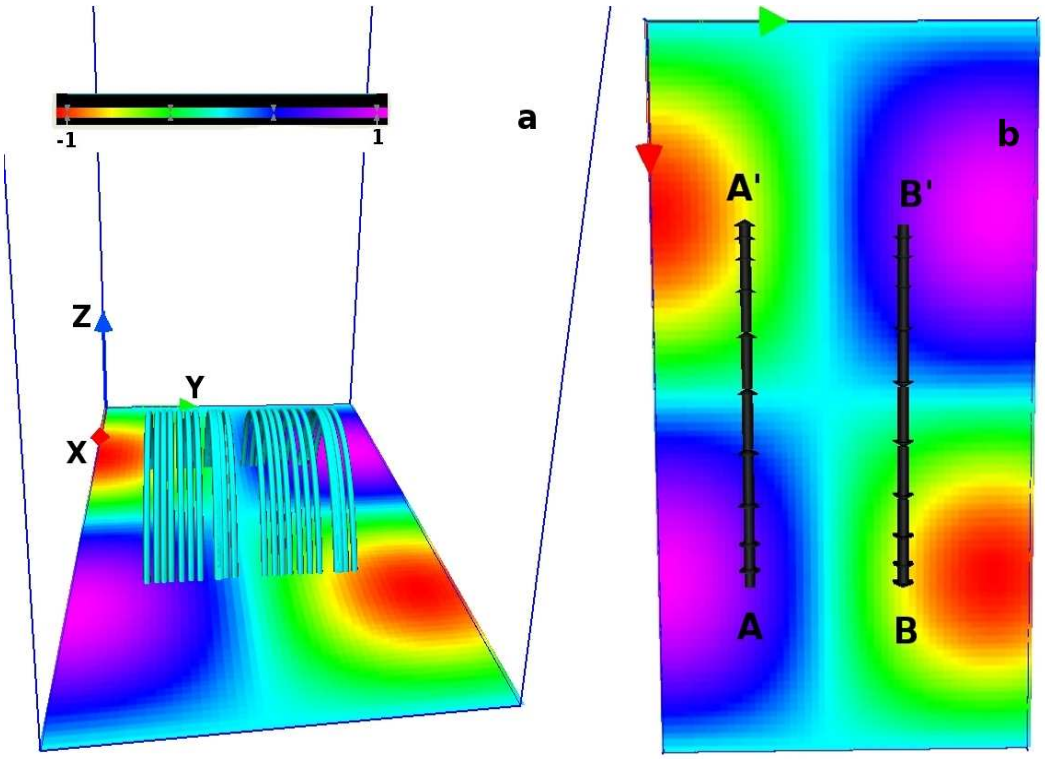

FIG. 1: (color online). Panel a represents the geometry of magnetic field lines for initial field $\mathbf{H}^1$. In panel b, we plot the projections of a selected pair of field lines on the $z = 0$ plane. The symbols A, A' and B, B' mark two opposite polarity footpoint pairs. The projections being straight lines, confirms that the field lines for $\mathbf{H}^1$ are untwisted. Both panels are overlaid with contours of H_z^1 to indicate the polarities of footpoints.

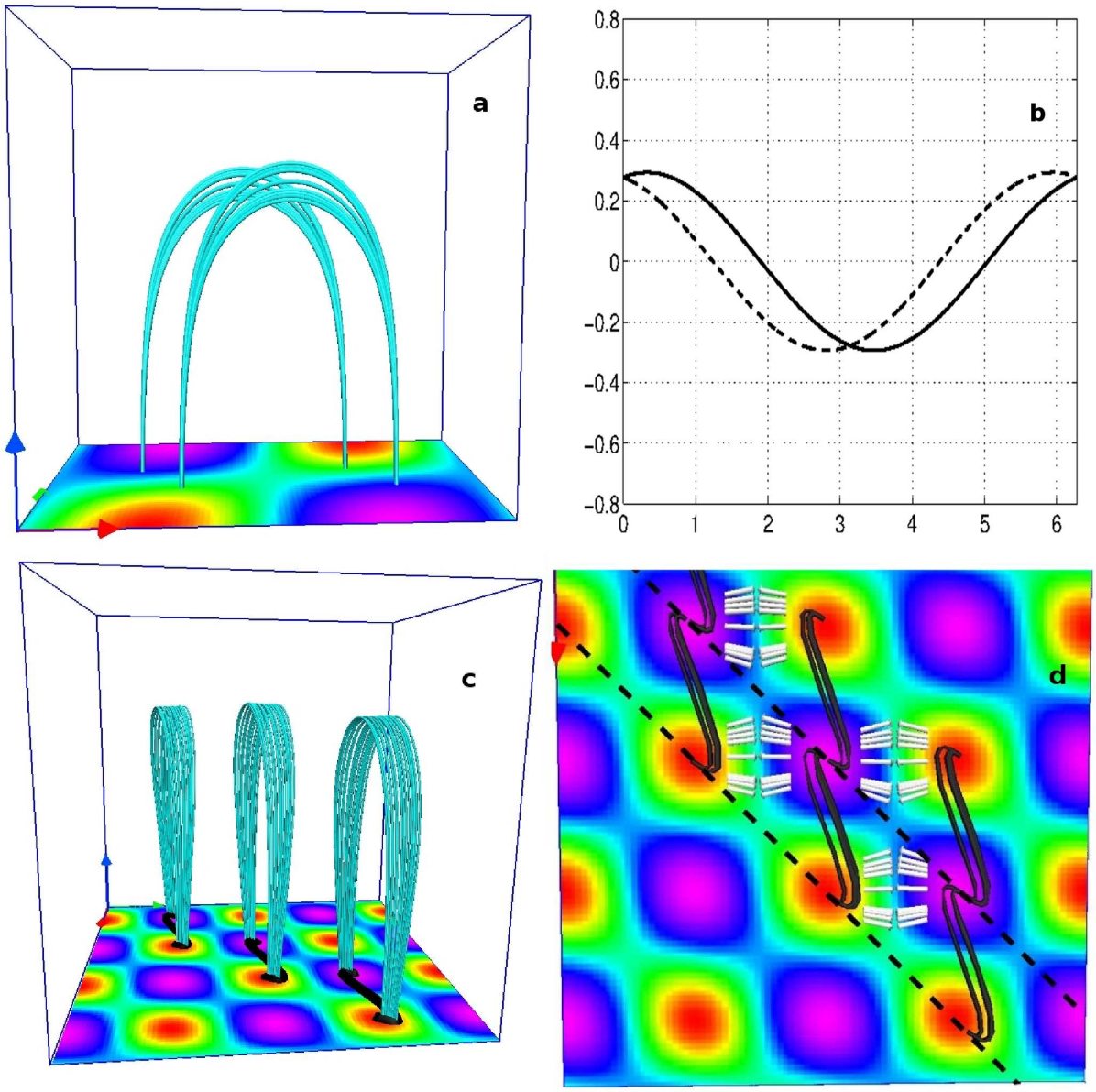

FIG. 2: (color online). Panels a and c illustrate the field lines for initial fields $\mathbf{H}^2$ and $\mathbf{H}^3$ respectively, overlaid with contours H_z^2 and H_z^3. Noteworthy is the projections of field lines (in black) of $\mathbf{H}^3$ on the $z = 0$ plane — to be curved lines, which confirms the corresponding field lines to be twisted. Panel b plots $H_x^2(x, y, 0)$ (solid line) and $-H_x^2(x, \pi - y, 0)$ (dashed line) with x, for $y = 2\pi/5$. The relative displacement of these two curves gives the shift $\Delta x = \pi/5$. In panel d, we re-plot the projections of $\mathbf{H}^3$ (in Black) on the $z = 0$ plane overlaid with the vector plots of horizontal component of the Lorentz force $\mathbf{L}^3$ (in Gray). The intersections of the dashed lines with the projections, mark the locations of footpoints of $\mathbf{H}^3$.

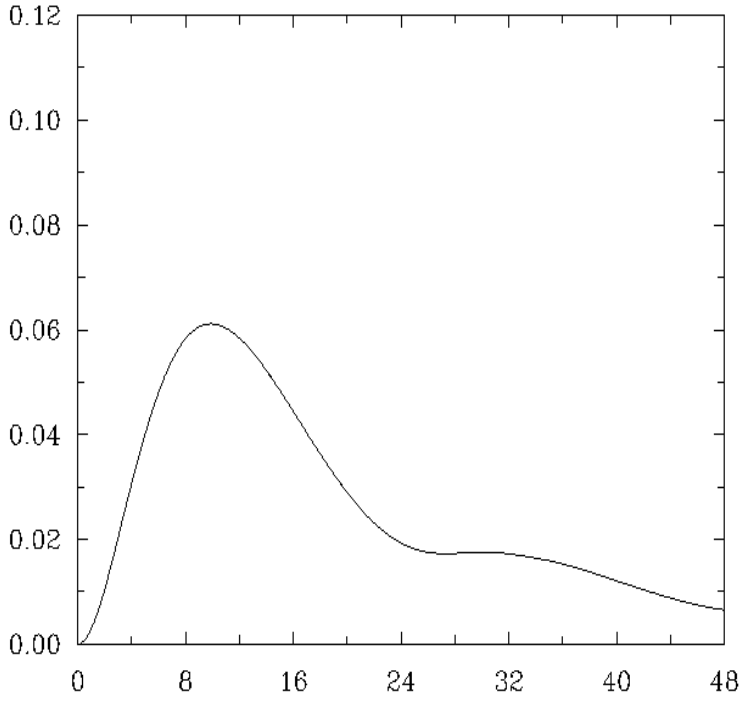

FIG. 3: (color online). History of kinetic energy (normalized to the total initial energy) as the magnetofluid relaxes from the initial state $\mathbf{H}^1$. The abscissa is in seconds whereas the ordinate is dimensionless. Important are development of the peak at $t = 8$ s and the quasi-steady phase of evolution for $t \in (24, 32)$ s.

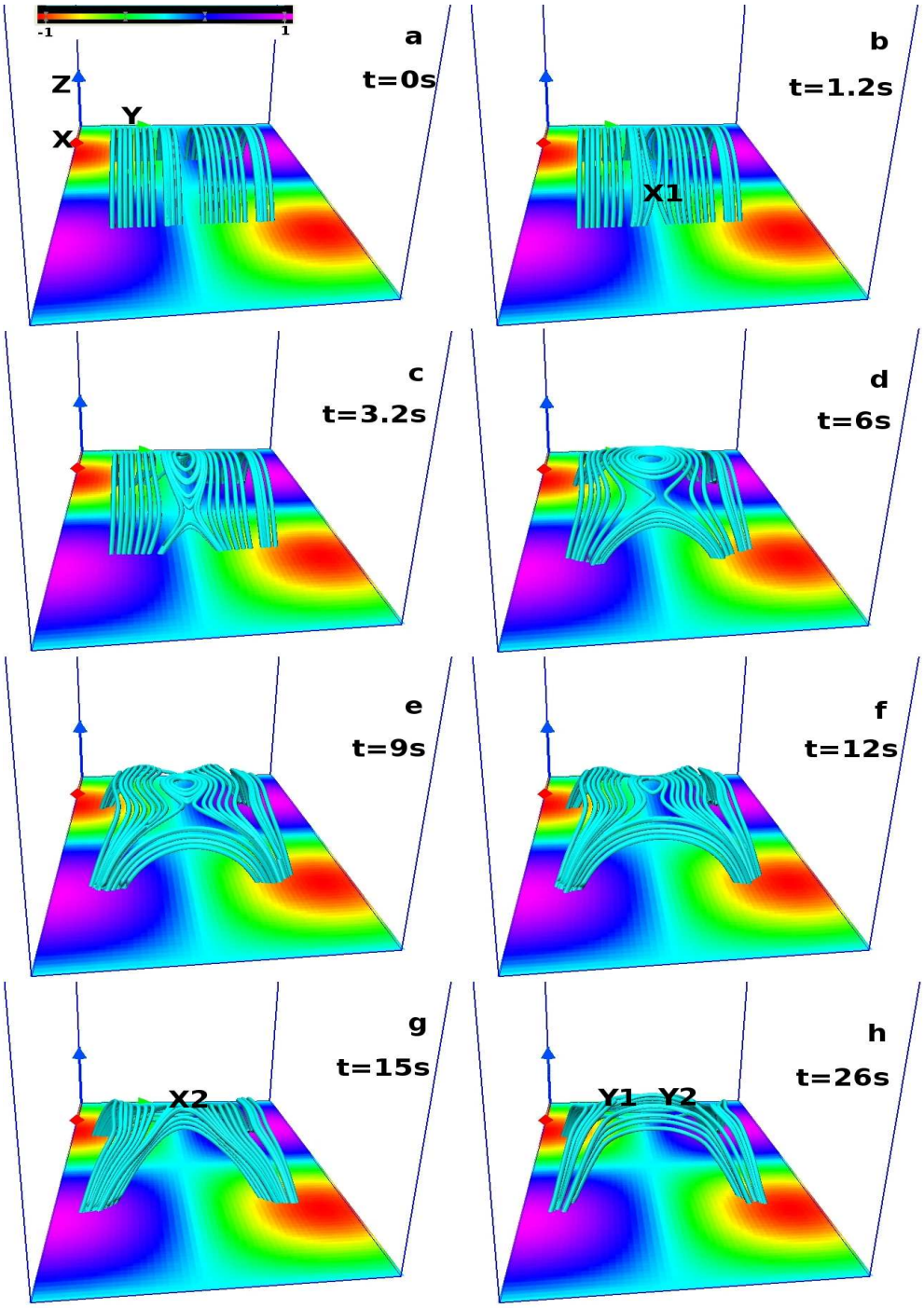

FIG. 4: (color online). Magnetic field lines of $\mathbf{H}^1$ in their important phases of evolution. Each panel of the figure is further overlaid with contours of H_z^1 at the $z = 0$ plane. Noteworthy are the formations of two X-type nulls (one of the nulls is marked with symbol X1 in panel b), and magnetic island which is most prominent in panel d. Panels g and h mark the onset of a new X-type null (denoted by the symbol X2) which is further squashed into two Y-type neutral points (marked with symbols $Y1$ and $Y2$) at $t = 26$ s. We also note, this generation of two Y-type nulls are concurrent with the quasi-steady phase of the evolution.

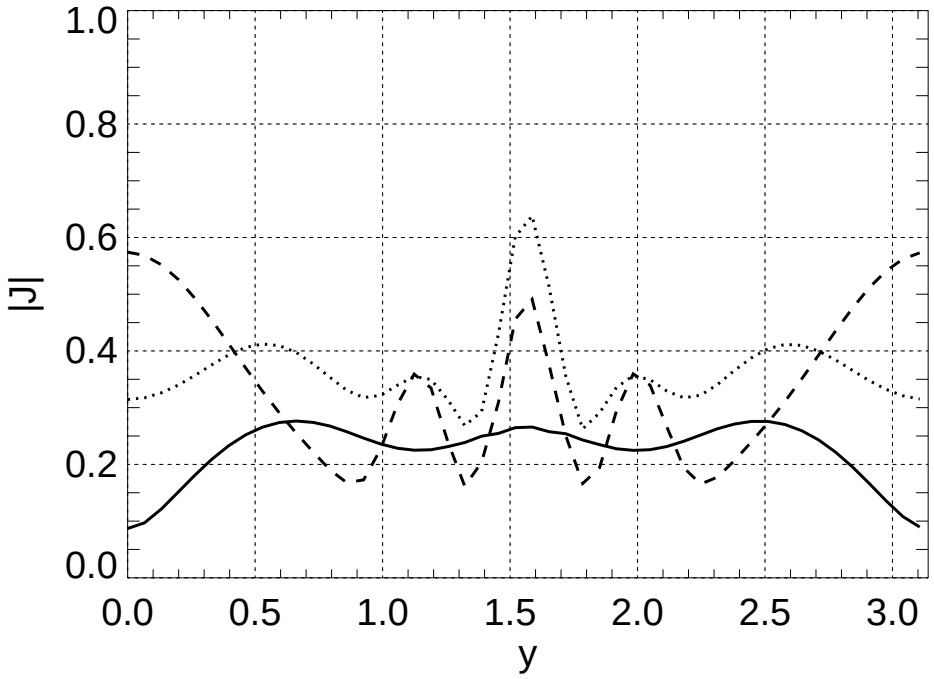

FIG. 5: (color online). Variation of current density | **J** | with y at three time instants; $t = 0s$ (solid line), $t = 1.2s$ (dotted line) and $t = 2.5s$ (dashed line). The plotted | **J** | is calculated for $x = 3\pi/2, z = 0$. The observed rise and fall of | **J** | at the field reversal layer $y = \pi/2$ is indicative of a CS formation and its subsequent decay.

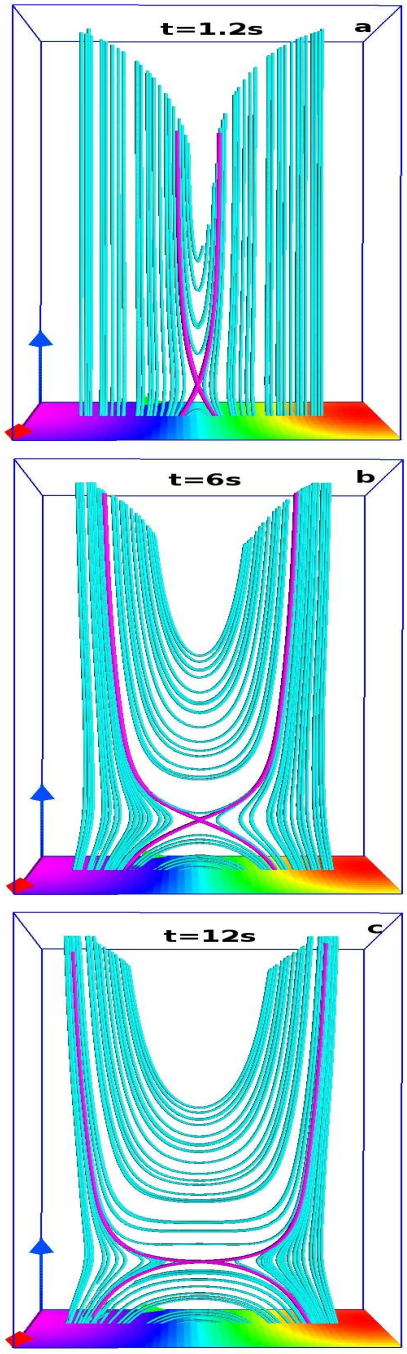

FIG. 6: (color online). Snapshots of field lines for $\mathbf{H}^1$, projected on the $x = 3\pi/2$ plane. Noticeable is the ascend of the X-type neutral point (separatrices of which are drawn in magenta), with time. Also, footpoint separations of reconnected field lines show a concurrent increase in the y direction.

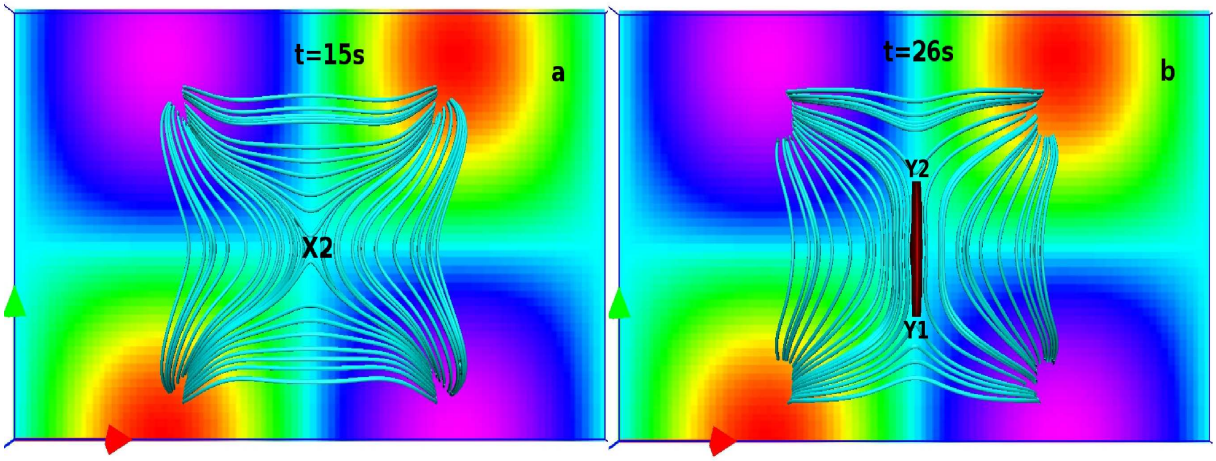

FIG. 7: (color online). Top view of panels g and h of figure 4. The developments of a new X-type null ($X2$ in panel a) and an extended CS (depicted in color red in panel b) is evident.

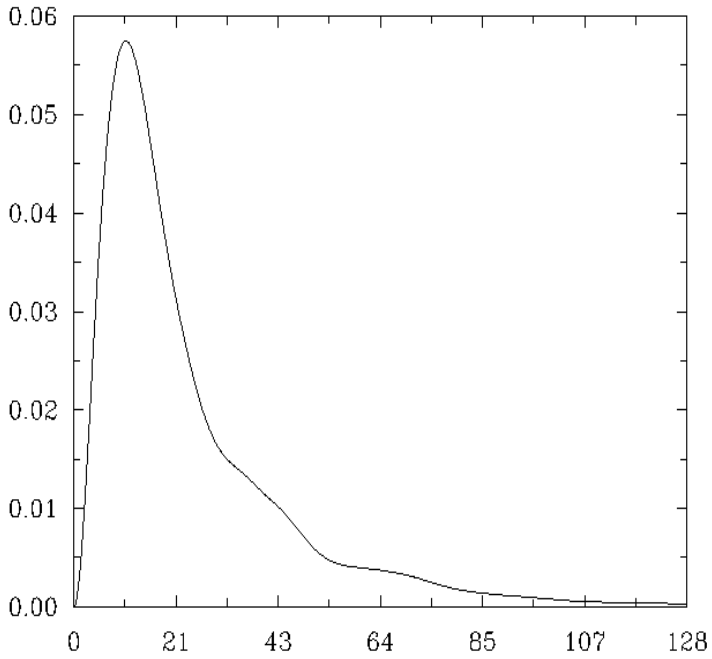

FIG. 8: (color online). History of kinetic energy (normalized to the total initial energy) for the relaxation from the initial state $\mathbf{H}^2$. The abscissa is in seconds and the ordinate is dimensionless. Important are, development of the peak at $t \approx 10s$, the quasi-steady phase of evolution for $t \in (53, 75)$ s and the subsequent monotonic decay of the kinetic energy.

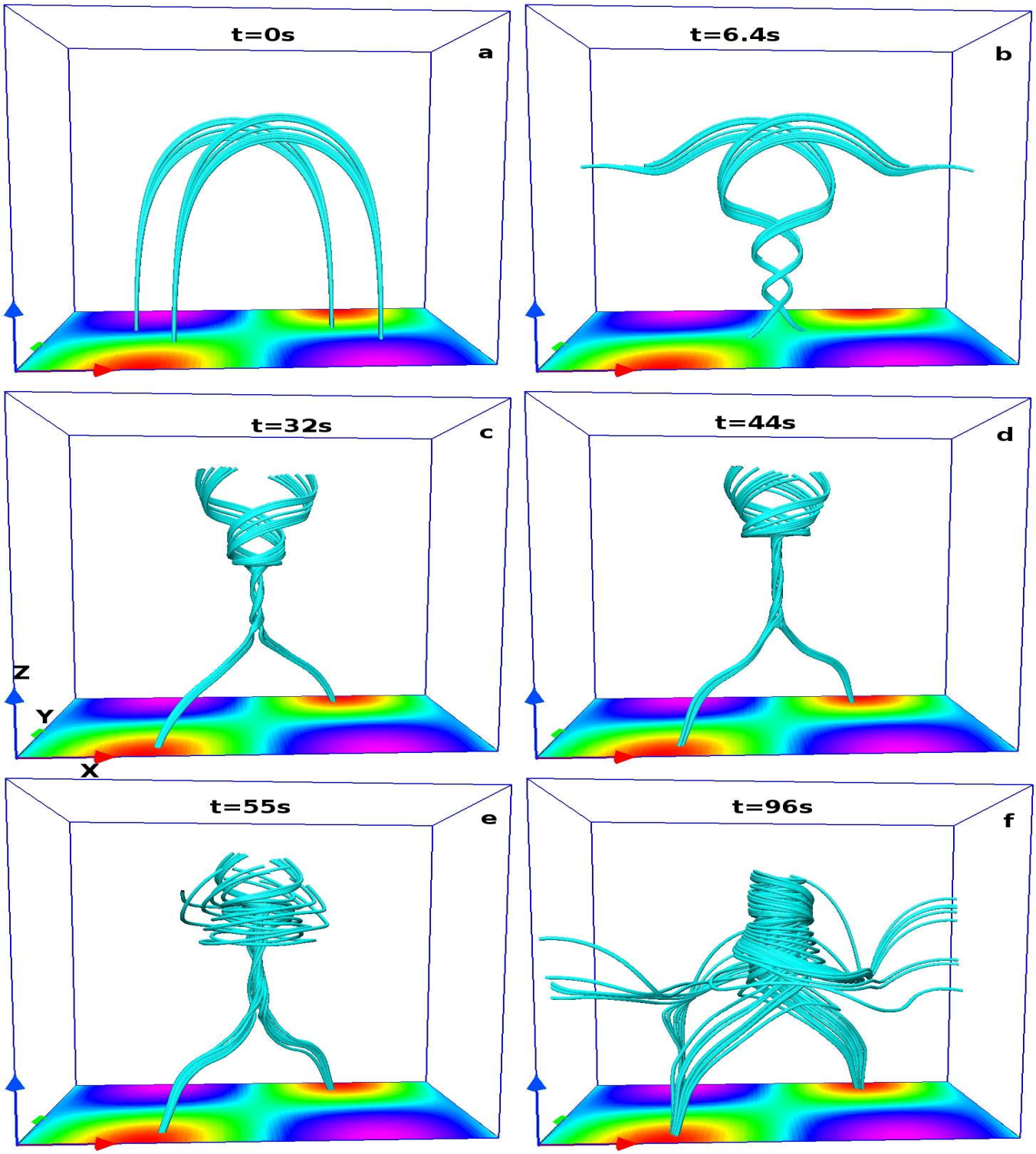

FIG. 9: (color online). Instances of magnetic field lines with $\mathbf{H}^2$ as the initial magnetic field. The overlaying H_z^2 contours indicate the glide symmetry of the opposite polarity footpoints situated across the mirror plane $y = \pi/2$. The sequential development of helical field lines, akin to solar tornadoes, is illustrated in panels b to d. Panels e and f represent the "untwisting" motion of the already developed helical field lines illustrated in panel d.

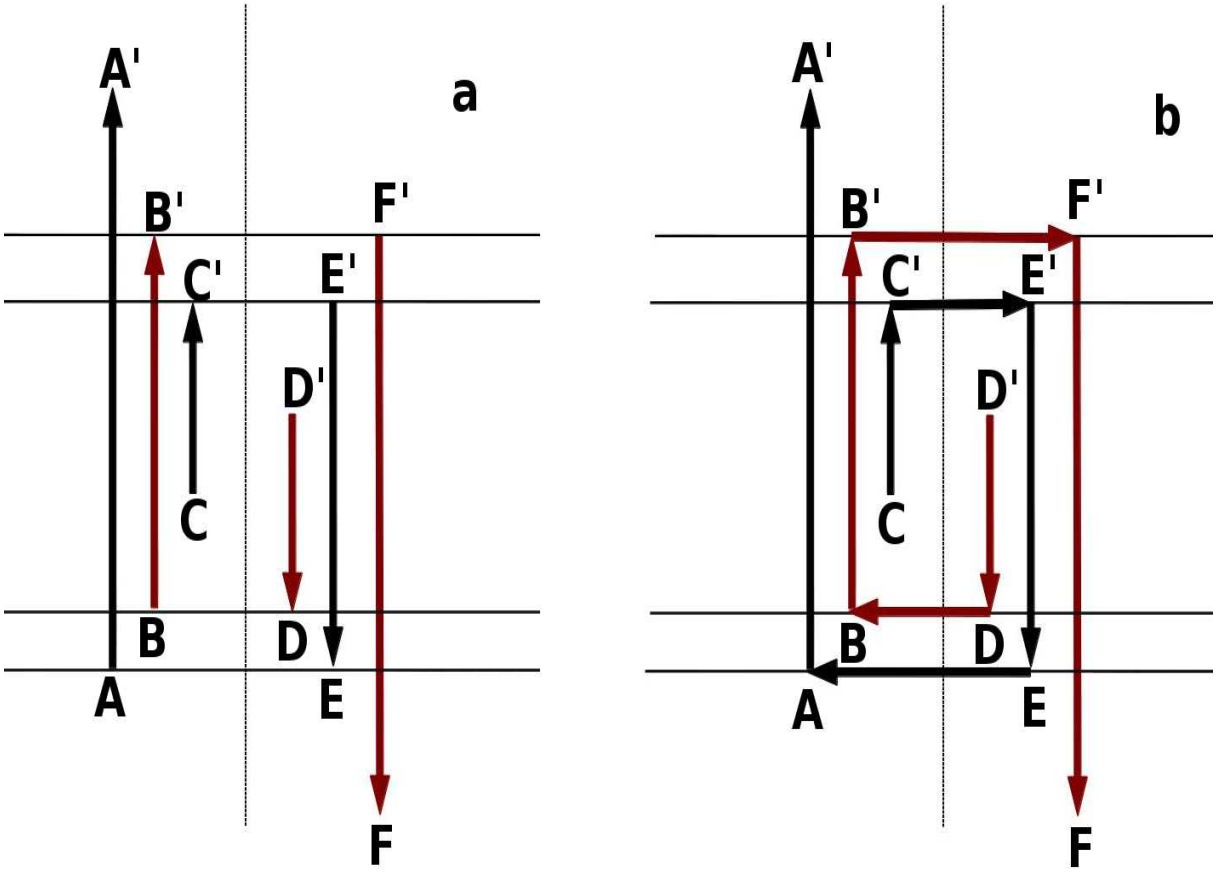

FIG. 10: (color online). The panel a depicts a schematic of the initial field lines for $\mathbf{H}^2$, projected on the $z = 0$ plane. The corresponding footpoints are marked by the pairs A, A'; B, B'; C, C'; D, D'; E, E'; and F, F' respectively. The glide plane is represented by the dotted line situated at the middle. In panel b, the horizontal arrows connect a pair of reconnecting footpoints with opposite polarity.

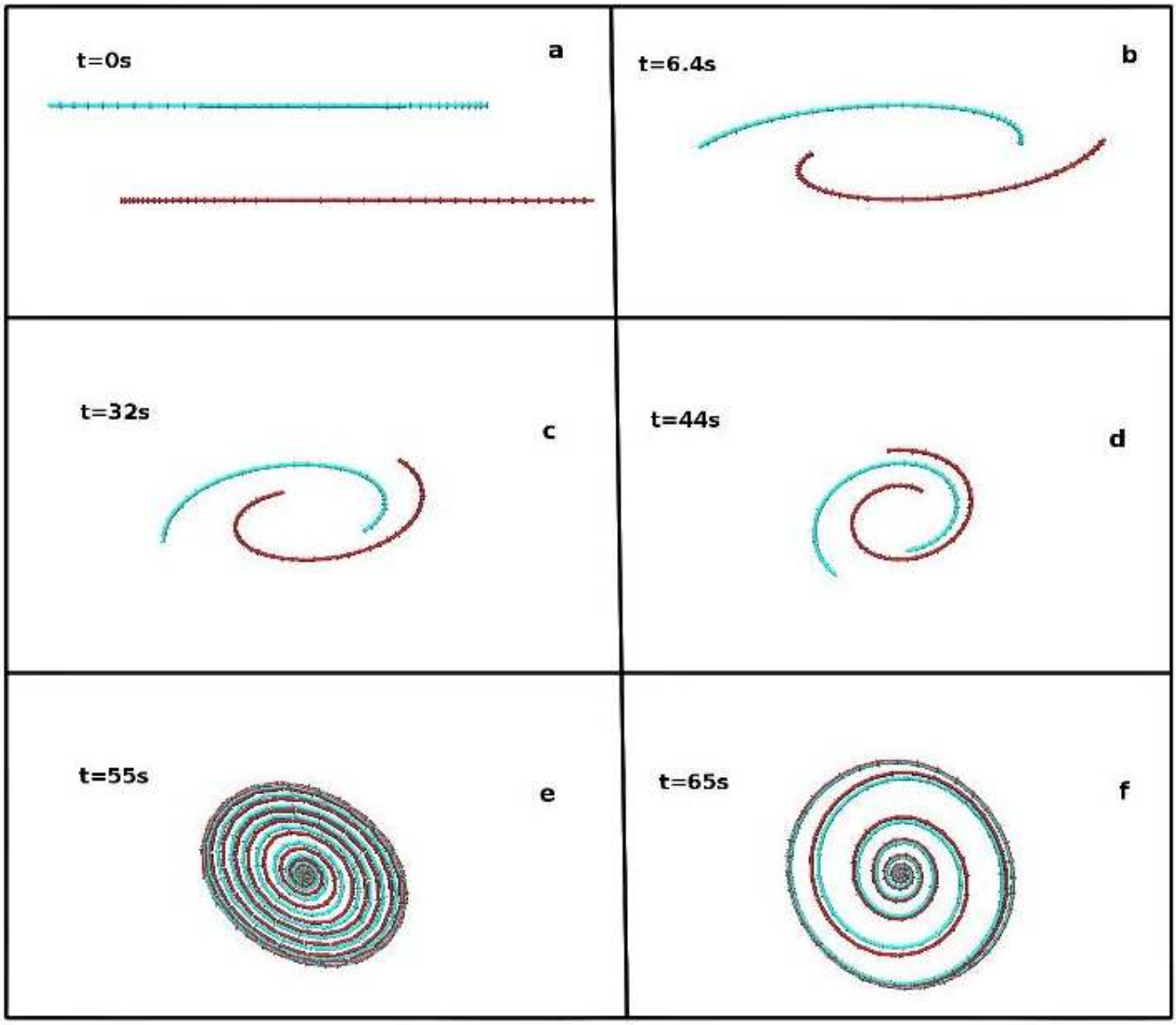

FIG. 11: (color online). The evolution of a pair of glide-symmetric field lines for the field $\mathbf{H}^2$, projected on the $z = \pi/2$ plane. The development of two complementary spirals of similar chiralitity indicates the three dimensional field lines to be helices. Further we note that throughout their evolution, these complementary spirals are in the same direction and hence the geometry of field lines are not favorable for CS formations. The relative decrease in density of field lines at $t = 55$ s (panel e) and $t = 65$ s (panel f) is due to the untwisting motion.

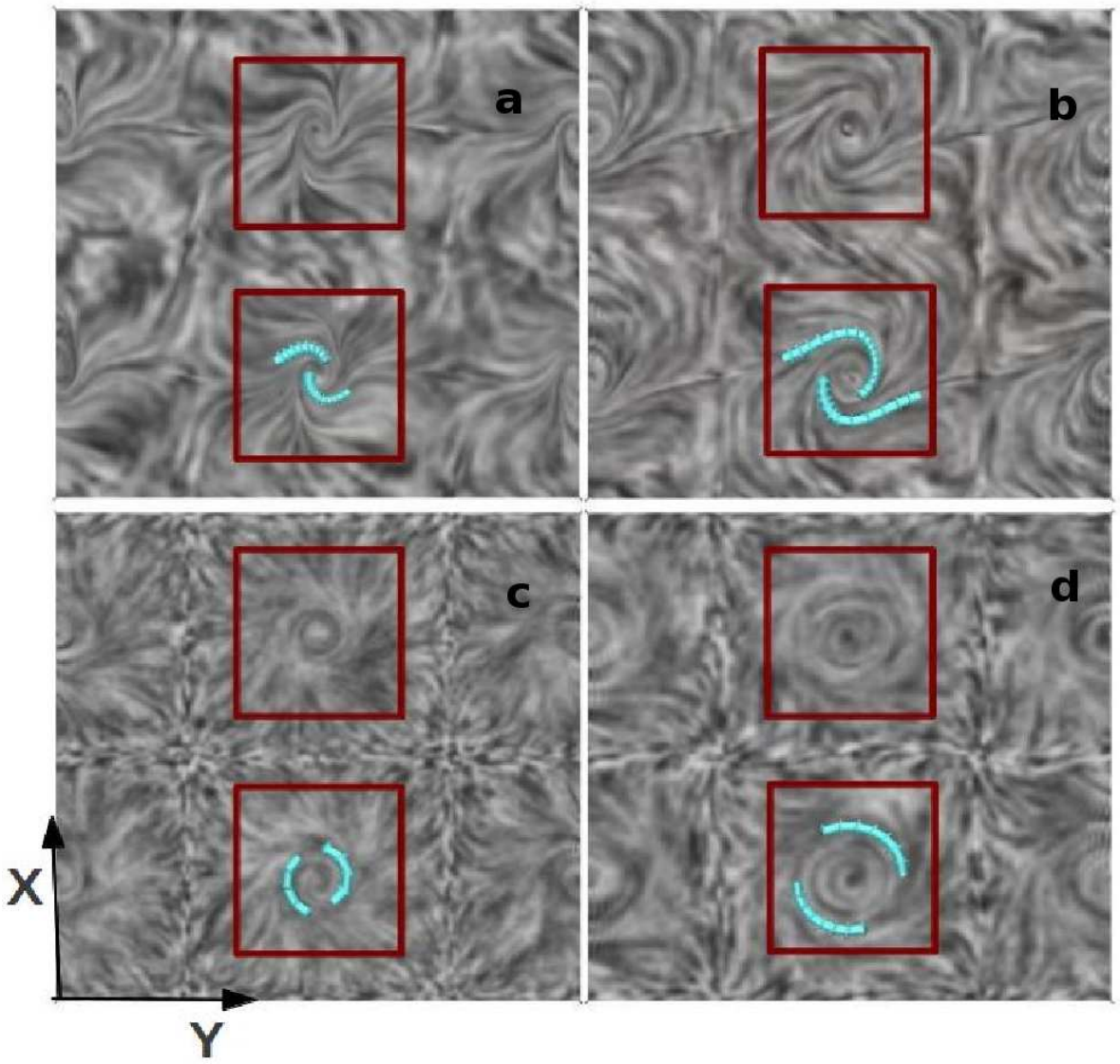

FIG. 12: (color online). The flow images of the velocity generated by the Lorentz force $\mathbf{L}^2$. The panels a and b depict concurrent images ($t = 44$ s) at heights $z = 3\pi/5$, and $6\pi/5$ respectively, overlaid with velocity field lines (in cyan) projected on the corresponding z-constant levels. Noteworthy are the rotation of the fluid in a clockwise direction as marked by the directions of the plotted velocity field lines; and the increment in size of vortices with height which confirms the development of a funnel shaped structure. In panels c and d, flow images at same heights but later instant $t = 96$ s are shown. The direction of the overlaid velocity field lines (in cyan) show an anticlockwise rotation of the fluid. Here the y coordinate ranges from 0 to 2π.

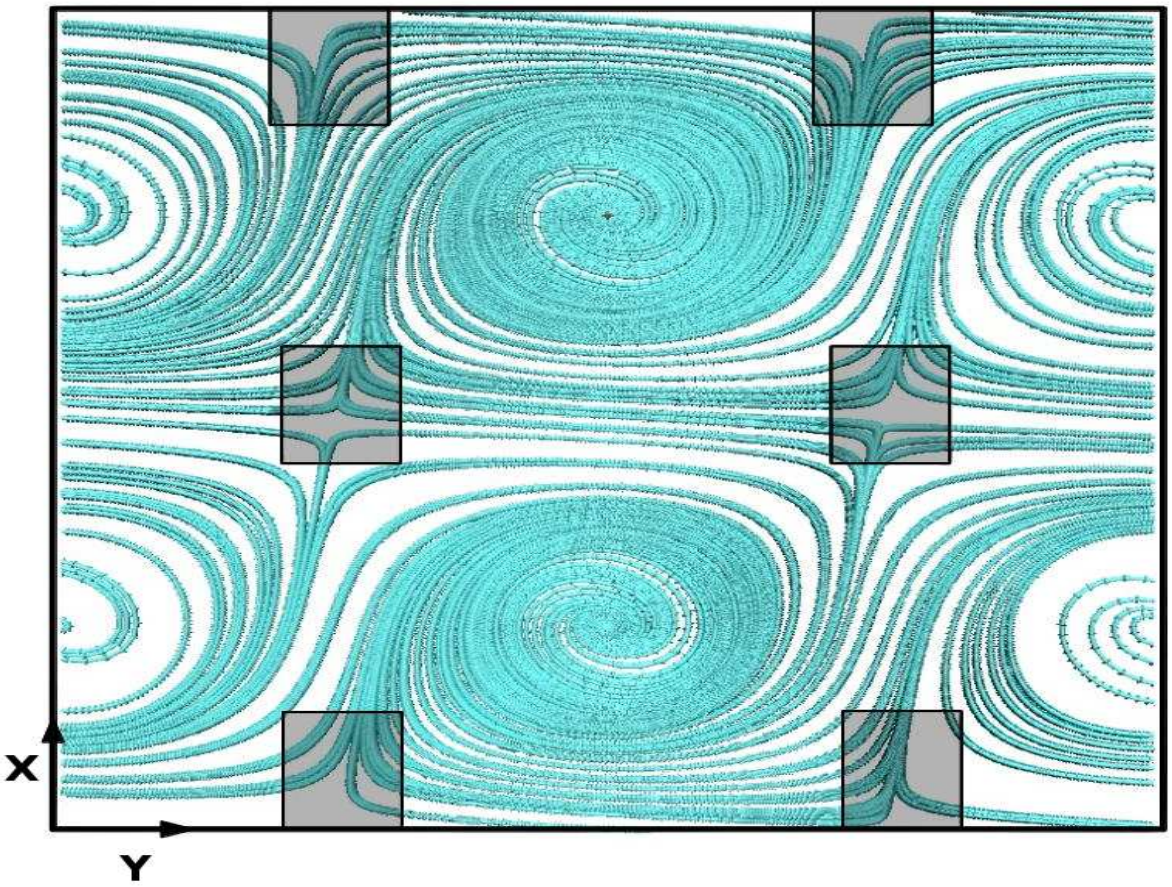

FIG. 13: (color online). Plot of magnetic field lines at $t = 51$ s projected on the $z = 6\pi/5$ plane, extended from 0 to 2π in the y direction. The rectangular patches represent reconnection regions.

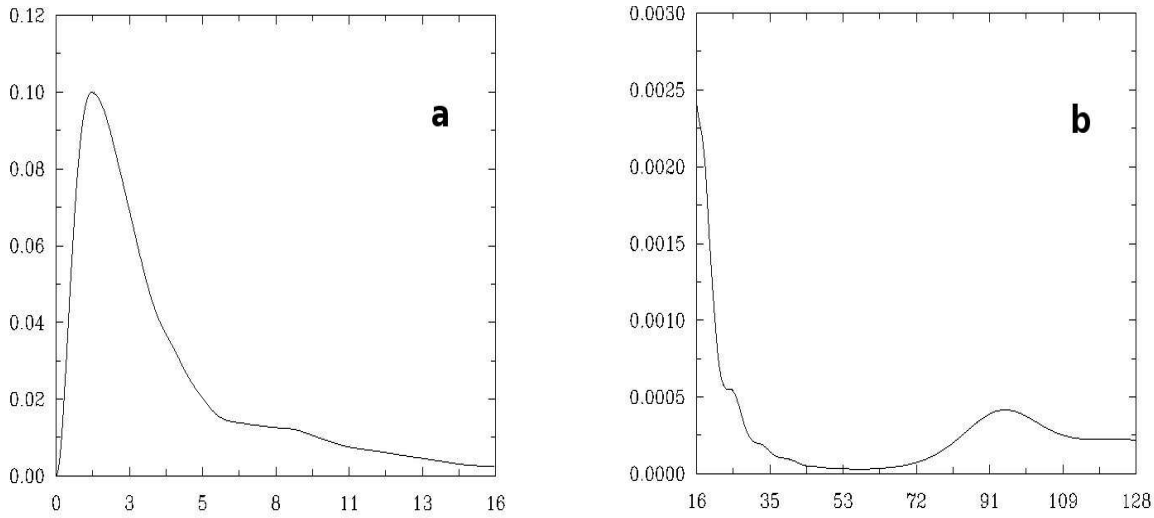

FIG. 14: (color online). Time evolution of kinetic energy of the magnetofluid (normalized to the initial total energy) as the fluid relaxes from the initial field $\mathbf{H}^3$. Panels a and b depict the evolution in two consecutive overlapping ranges. The important features are; the formation of first peak in kinetic energy at $t \approx 1.5$ s, quasi-steady evolution in the period $t \in (44, 72)$ s, and development of a second peak in kinetic energy at $t \approx 91$ s.

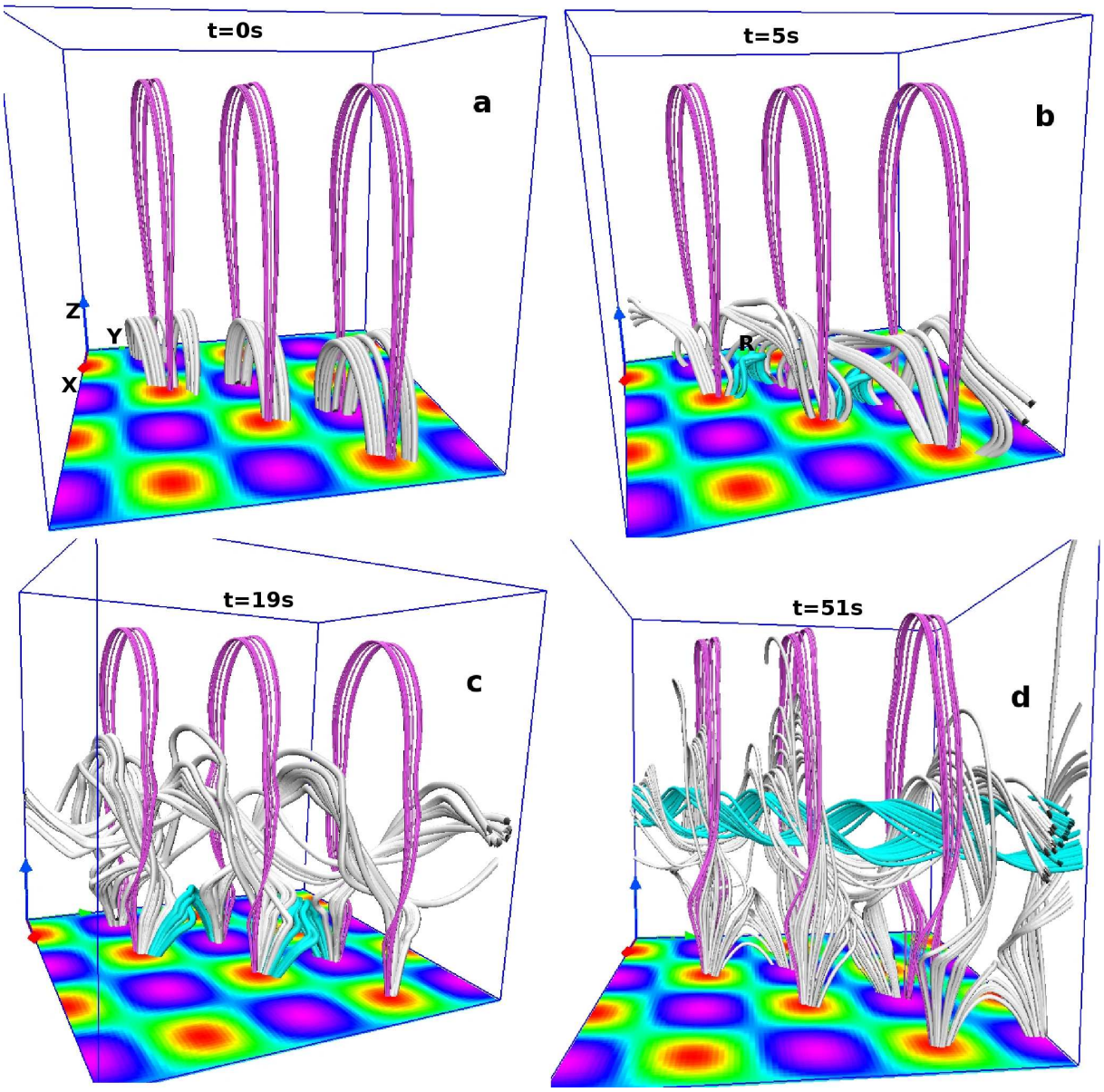

FIG. 15: (color online). Snapshots of magnetic field lines in their evolution where $\mathbf{H}^3$ is the initial magnetic field. The magneta colored field lines have footpoints located almost at the sites where $\mid H_z^3 \mid$ is maximum, whereas the lower lying field lines (in Gray) have footpoints considerably away from these maximums. Noteworthy are the formations of helical field lines resembling a twisted flux rope, depicted in color cyan at panel d.

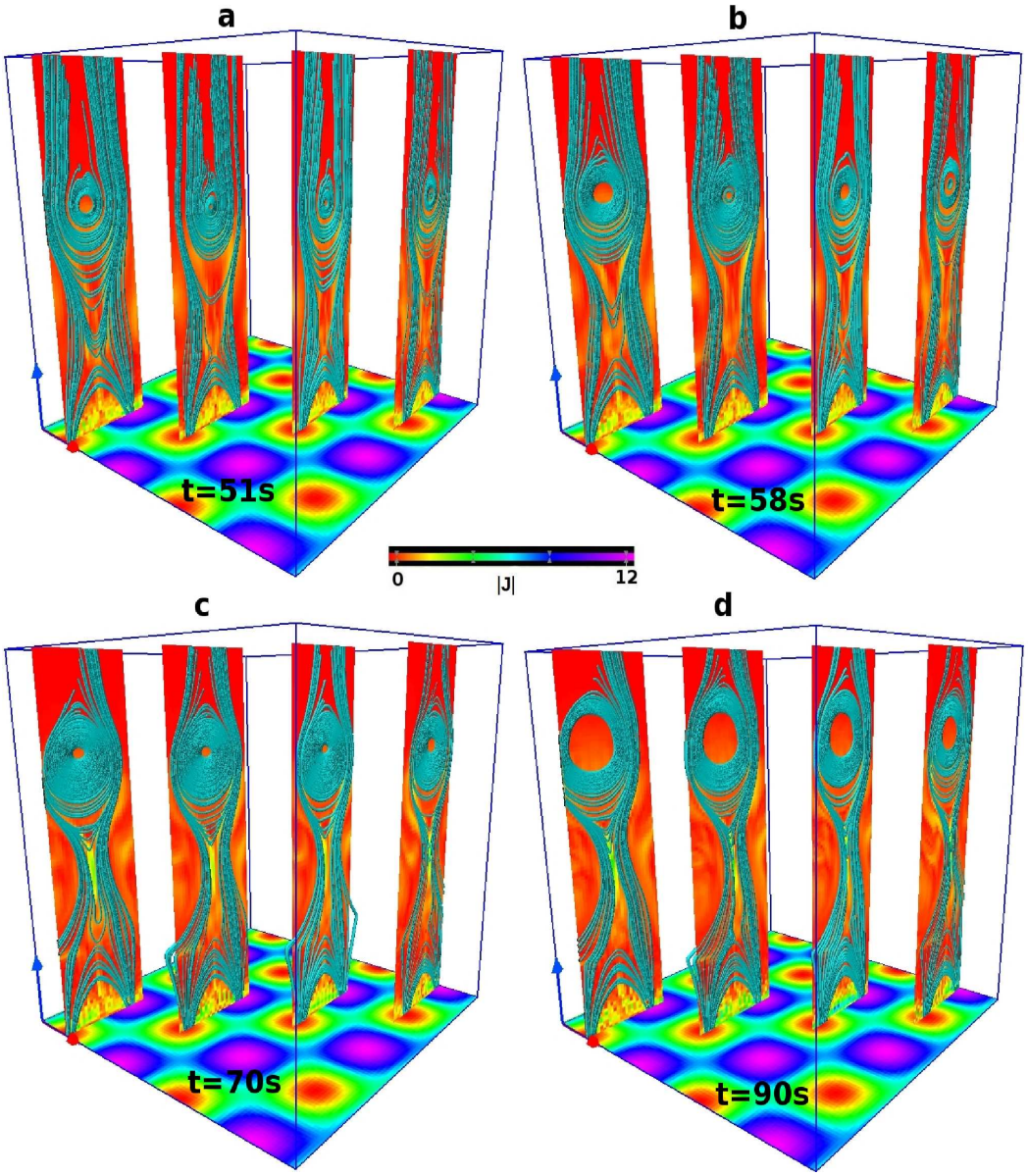

FIG. 16: (color online). Time sequence of field lines in their evolution from the initial field $\mathbf{H}^3$ at the instances $t = 51$ s, $t = 58$ s, $t = 70$ s and $t = 90$ s, projected on x-constant planes. The intersections of the flux rope with these planes are identified by the closed field lines. Noteworthy are the ascend of the closed field lines, and hence the flux rope, with time along with the formation of an extended CS represented in Green. Also important is the observation that the onset of the extended CS is simultaneous with the quasi-steady phase of the evolution.